JOC The Journal of Organic Chemistry

Article

pubs.acs.org/joc

Thermal- and pH-Dependent Size Variable Radical Nanoparticles and Its Water Proton Relaxivity for Metal-Free MRI Functional Contrast Agents

Kosuke Morishita,[†] Shuhei Murayama,[§] Takeru Araki,[†] Ichio Aoki,[§] and Satoru Karasawa*[,†,‡]

[†]Graduate School of Pharmaceutical Sciences, Kyushu University, 3-1-1 Maidashi, Higashi-Ku, Fukuoka, 812-8582, Japan

[‡]PRESTO, Japan Science and Technology Agency, Kawaguchi 332-0012, Japan

[§]Department of Molecular Imaging and Theranostics, National Institute of Radiological Sciences (NIRS), QST, Anagawa 4-9-1, Inage, Chiba-city 263-8555, Japan

Supporting Information

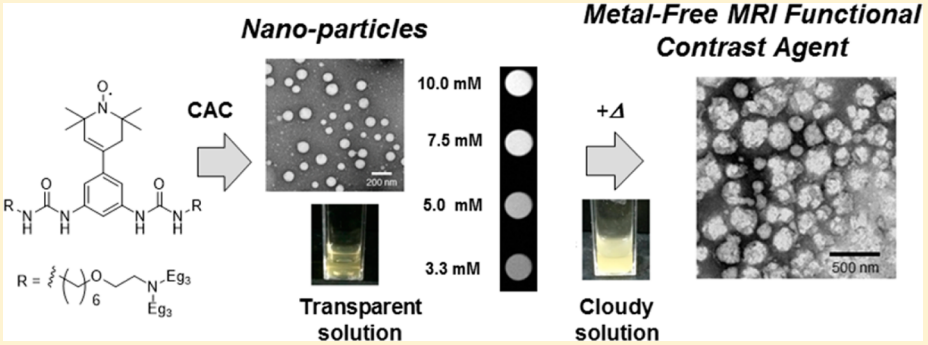

ABSTRACT: For development of the metal-free MRI contrast agents, we prepared the supra-molecular organic radical, **TEMPO-UBD**, carrying TEMPO radical, as well as the urea, alkyl group, and phenyl ring, which demonstrate self-assembly behaviors using noncovalent bonds in an aqueous solution. In addition, **TEMPO-UBD** has the tertiary amine and the oligoethylene glycol chains (OEGs) for the function of pH and thermal responsiveness. By dynamic light scattering and transmission electron microscopy imaging, the resulting self-assembly was seen to form the spherical nanoparticles 10−150 nm in size. On heating, interestingly, the nanoparticles showed a lower critical solution temperature (LCST) behavior having two-step variation. This double-LCST behavior is the first such example among the supra-molecules. To evaluate of the ability as MRI contrast agents, the values of proton (^{1}H) longitudinal relaxivity (r_1) were determined using MRI apparatus. In conditions below and above CAC at pH 7.0, the distinguishable r_1 values were estimated to be 0.17 and 0.21 mM^{-1} s^{-1}, indicating the suppression of fast tumbling motion of TEMPO moiety in a nanoparticle. Furthermore, r_1 values became larger in the order of pH 7.0 > 9.0 > 5.0. Those thermal and pH dependencies indicated the possibility of metal-fee MRI functional contrast agents in the future.

INTRODUCTION

Magnetic resonance imaging (MRI) is widely used as a noninvasive diagnostic method because of its properties of safety and deep penetration into the body.[1] To obtain bioimages emphasizing for specific tissues such as a tumor tissue, contrast agents (CAs) are often used. Currently, gadolinium (Gd) complexes are widely used as CAs because Gd ions have the largest spin quantum number of all the elements.[2] However, Gd complex CAs have potential side-effects such as renal disorder[3] due to the free Gd ion and a lack of specificity to the tissues. In addition, recently, accumulation in the brain, especially among children, was reported,[4] so the replacement of Gd complexes by new CAs is strongly desired. Stable organic radicals such as TEMPO are widely used as probes for bio-ESR imaging,[5] spin-trap against reactive oxygen species (ROS),[6] and so on. Such organic radicals can function as MRI CAs due to their possession of electron spin. However, their water proton relaxivity values (r_1 and r_2) are considerably smaller than those of Gd complexes.[7] To increase the relaxivity value, taking advantage of the suppression of fast tumbling of the TEMPO moiety rotational correlation time (τ_R) by enlarging the molecular size is a promising approach studied by many groups.[8] We previously reported that nanoparticles with ∼10 nm size consisting of amphiphilic oligonucleotides carrying TEMPO exhibited an unexpectedly large r_1 value compared to Gd complexes.[9] The resulting behavior was based on a slower molecular motion of the nanoparticles and effective assembly of the water molecules against the TEMPO moiety. The exhibited high relaxivity indicated that using CAs with radicals is a promising method for development of metal free CAs.[10] Separately, we reported that water-soluble supra-molecules consisting of urea benzene

Received: June 23, 2016
Published: August 19, 2016

DOI: 10.1021/acs.joc.6b01509
J. Org. Chem. 2016, 81, 8351−8362

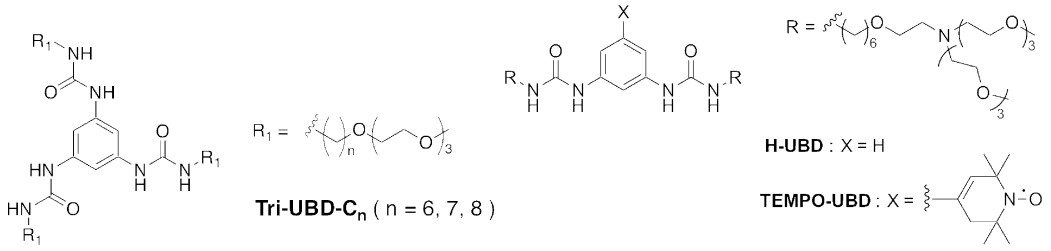

Figure 1. Molecular structures of **Tri-**, **H-**, and **TEMPO-UBD**.

Scheme 1. Synthesis Routes of H- and TEMPO-UBD

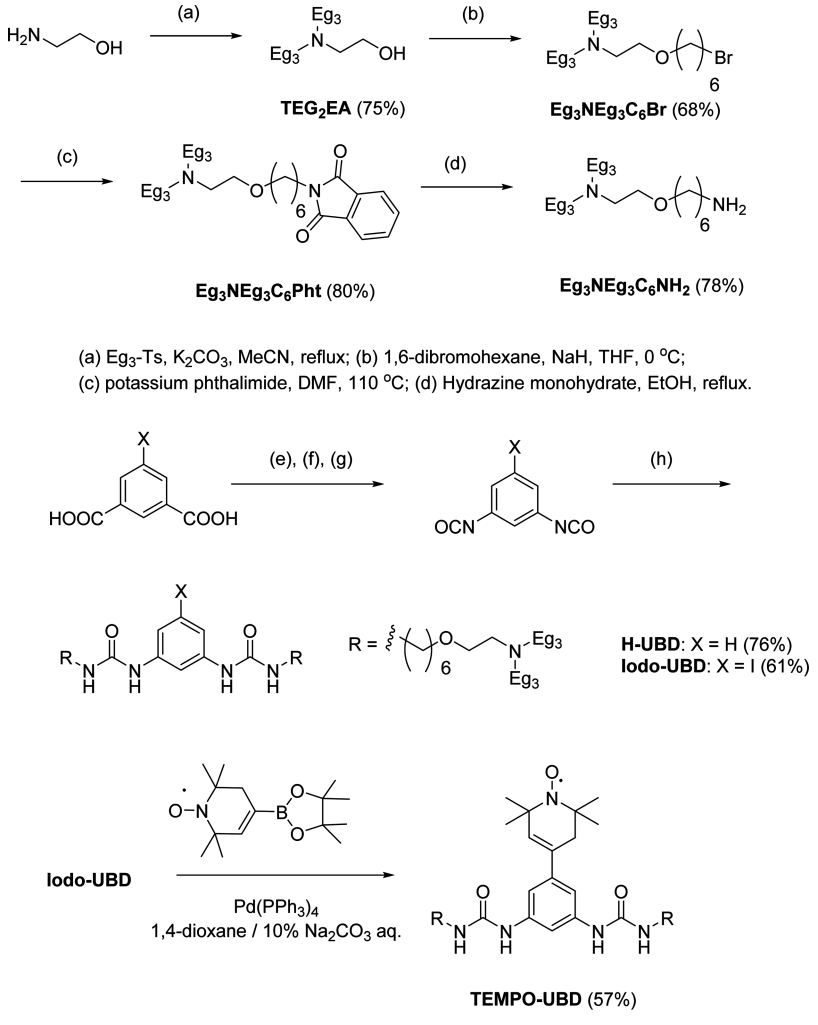

frameworks (UBDs) having oligoethylene glycol chains (OEGs) showed thermal responsiveness in water solution (Figure 1).[11] Upon heating the solution, an abrupt self-assemble behavior with low temperature critical temperature (LCST)[12] took place due to the dehydration surrounding OEGs, forming microsize particles. This LCST property is rare for supra-molecules.[13] This time, UBDs carrying TEMPO (**TEMPO-UBD**) as well as tertiary amino groups were prepared, and thermal responsive behaviors accompanied by LCST and structural changes in solution were revealed. Furthermore, to confirm the driving force of the self-assembly of UBDs in water solution, UBD without TEMPO (**H-UBD**) as a hydrophobic moiety was prepared as reference compound and carefully compared to **TEMPO-UBD**. Using **TEMPO-UBD**, the water proton relaxivity values, r_1 and r_2, were determined under the conditions between pH 5.0 and 9.0. We herein describe the variations of physical properties and morphologies in response to various stimuli and evaluate the candidacy for metal-free MRI functional CAs. The molecular structures of **Tri-**, **H-**, and **TEMPO-UBD** are shown in Figure 1.

RESULTS AND DISCUSSION

Syntheses of H- and TEMPO-UBD (Scheme 1). A primary amine analogue having an amphiphilic side chain ($Eg_3NEg_3C_6NH_2$)[14] was synthesized in three steps from 2-

DOI: 10.1021/acs.joc.6b01509
J. Org. Chem. 2016, 81, 8351−8362

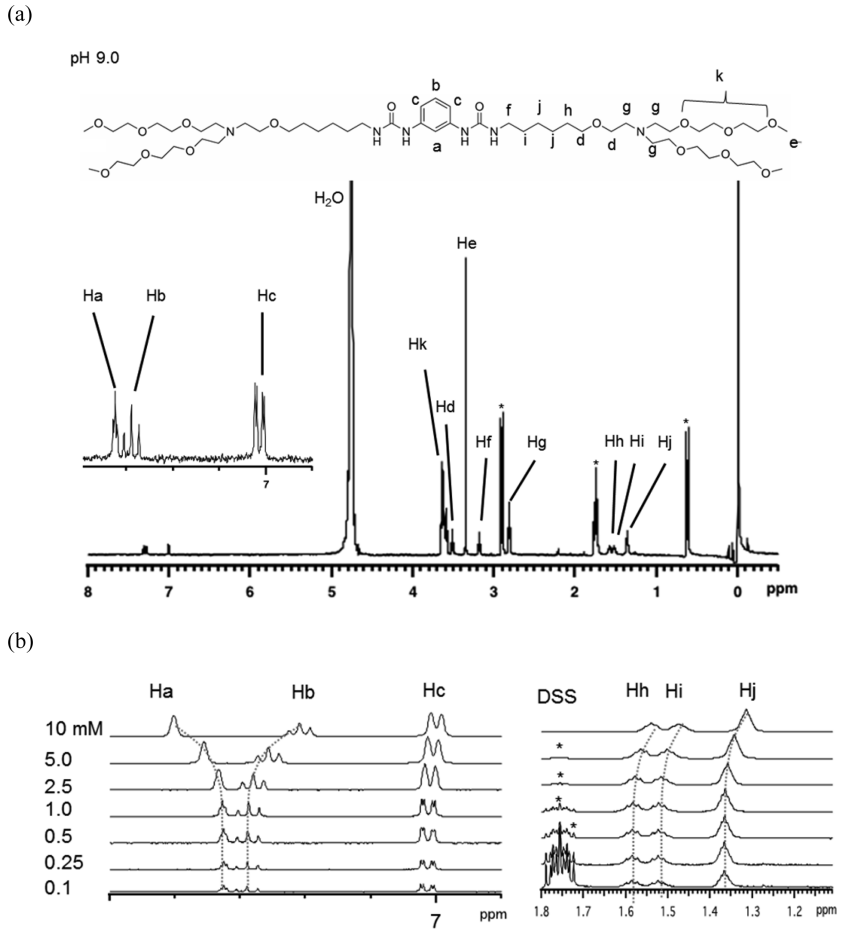

Figure 2. (a) ^{1}H NMR spectra of **H-UBD** in 0.1 mM buffer solution at pH 9.0. (b) Concentration dependence of **H-UBD** in buffer solution at pH 9.0 in the expansions of aromatic (left) and alkyl chain (right) regions. Hxs indicate the protons corresponding the molecular structure of **H-UBD** (upper). The dotted blue lines represent the fitting curves according to the isodesmic model (see text). The asterisks denote the proton of DDS as standard material.

aminoethanol as the starting materials via a tertiary amine with bistriethylene glycol at the amino group (**TEG$_2$EA**), an amphiphilic compound (**Eg$_3$NEg$_3$C$_6$Br**), and a phtalimide having the amphiphilic chain (**Eg$_3$NEg3C6Pht**). The resulting **Eg$_3$NEg$_3$C$_6$NH$_2$** was coupled with 1-iodo-3,5-diisocyanatobenzene, to afford the diurea derivative having the amphiphilic chain (**Iodo-UBD**) as a colorless oil. The radical analogue having the amphiphilic chain (**TEMPO-UBD**) was prepared by Suzuki–Miyaura coupling[15] between **Iodo-UBD** and the TEMPO analogue having the boronic acid pinacolato ester.[16] The analogue **H-UBD** without TEMPO radical as the reference compound was prepared in a manner similar to **TEMPO-UBD** but using isophthalic acid in place of 5-iodoisophthalic acid. The synthesis routes of **H-** and **TEMPO-UBD** are shown in Scheme 1.

Self-Assembly Behaviors of H- and TEMPO-UBD in Aqueous Solutions. To reveal the self-assembly behavior of **H-** and **TEMPO-UBD** in aqueous solutions, the concentration and the pH dependence of ^{1}H NMR for **H-UBD** and ESR for **TEMPO-UBD** were examined using 0.1−10 mM solutions at pH 9.0, 7.0, and 5.0 at 23 °C.

*^{1}H NMR of **H-UBD** in a Buffer Solution.* Before investigation of the self-assembly behavior, to determine the pK_a value for **H-UBD**, pH titration of the chemical shift was performed (Figure S15).[17,18] As the pH value decreased, the protons neighboring the N atom in the tertiary amino moiety were shifted downfield due to the protonation of amines.[19] The variation of the proton close to the N atom (H_g in Figure S15) was plotted with pH (Figure S16), and the pK_a value of **H-UBD** was determined to be 7.6 according to eq S1. This value indicates that the protonation of amines took place completely and partially at pH 5.0 and 7.0, respectively, but not at all at pH 9.0. **TEMPO-UBD**, having the same framework as **H-UBD**, may be expected to show a similar pK_a value.

In the lowest concentration of 0.1 mM buffer solution at pH 9.0, protons corresponding to the benzene ring (H_a, H_b, and H_c), oligoethylene glycol chains (OEGs)(H_d, H_e, H_g, and H_k) and the alkyl chains (H_f, H_h, H_i, and H_j) were observed at 7.3−7.0, 3.7−2.8, and 3.2−1.3 ppm, respectively (Figure 2a). As the concentration increased from 0.1 to 10 mM (Figure 2b), the protons at the aromatic region (H_a and H_b), neighboring a tertiary nitrogen (H_g), and alkyl chains (H_{h-j}) clearly shifted with the broadening. In contrast, the peaks corresponding to the OEGs showed little shifting. The observed upfield shifts of H_b, H_g, and H_{h-j} indicate the typical behaviors of formation of the aggregate due to the shielding effect among the molecules.[20] In contrast, a downfield shift was observed in H_a, which is the proton in ortho position of two urea groups, revealing the formation of a pseudohydrogen bond between H_a and O atoms in the carbonyl group of urea moiety (Figure S19b).[21] This interaction might be led by the formation of the aggregate, and a

DOI: 10.1021/acs.joc.6b01509
J. Org. Chem. 2016, 81, 8351−8362

similar deshielding of proton was observed in the analogue of **Tri-UBD**, as previously reported.[11]

The resulting chemical shifts of H_b, H_g, and H_j were plotted as functions of the concentration (Figures 3 and S19a). To evaluate

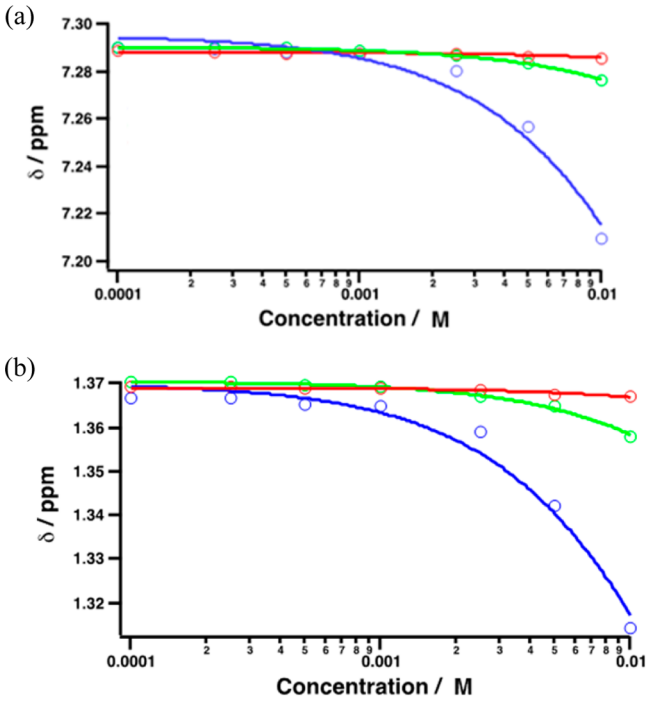

Figure 3. Plots of chemical shifts of H_b (a) and H_j (b) vs concentration for **H-UBD** at pH 9.0 (blue), 7.0 (green), and 5.0 (red). The solid lines indicate the theoretical curves according to the isodesmic model. See the text and Table 1.

the aggregation behavior, the shifting peaks were fitted according to the isodesmic model (eq S2),[22,23] to give association constants (K) of 12.3 ± 0.1, 54.3 ± 11.8, and 16.2 ± 0.1 M^{-1} in H_b, H_g, and H_j, respectively (Table 1). Furthermore, the inflection points in

Table 1. Values of Association Constants (K) Estimated from Isodesmic Model and CAC under Various Concentrations at pH 9.0, 7.0, and 5.0

	K values (M^{-1})			
pH	H_a	H_g	H_j	CAC (mM)
9.0	12.3 ± 0.1	54.3 ± 11.8	16.2 ± 0.1	0.5
7.0	4.03 ± 0.01	3.50 ± 0.01	4.31 ± 0.01	1
5.0	1.35 ± 0.01	1.28 ± 0.01	1.37 ± 0.25	5

the curvature suggested that the value of critical aggregation concentration (CAC) was 0.5 mM. Even though the concentration was over CAC and the aggregate was forming, the peaks corresponding to OEGs showed little shifting even at the highest concentration. This suggested that the OEGs were located outside the aggregate so the OEGs could move and/or rotate faster than the benzene ring and alkyl group. In neutral and acidic conditions at pH 7.0 and 5.0 of 0.1 mM, the obtained chemical shifts consisted of peaks at pH 9.0 except for H_g, which corresponded to the peak neighboring the tertiary N atoms (Figures S15 and S19a). Deshielding shifts of H_g were observed in the order pH 9.0 < 7.0 < 5.0, suggesting that the protonation took place at N atoms. In the plot of chemical shift vs concentration, even though concentration dependences similar to those at pH 9.0 were observed, the degree of change in the chemical shifts was smaller than for those at pH 9.0. The resulting K values in H_b, H_g, and, H_j, by fitting with the isodesmic model, were 4.03 ± 0.01, 3.50 ± 0.01, and 4.31 ± 0.01 M^{-1} at pH 7.0 and 1.35 ± 0.01, 1.28 ± 0.01, and1.37 ± 0.25 M^{-1} at pH 5.0. Comparing to the K values between various pH conditions, the estimated K values increased in the order pH > 9.0 > 7.0 > 5.0, suggesting that protonated **H-UBD** in acidic conditions was suppressed to form the aggregates owing to Coulomb repulsion and/or increased hydrophilicity. The CAC values under conditions at pH 7.0 and 5.0 were 1 and 5 mM, respectively. The ^{1}H NMR spectrum of **H-UBD** in 0.1 m M and the concentration dependence at pH 9.0 are shown in Figure 2a,b. Similar spectra at pH 7.0 and 5.0 are shown in Figure S17. The plots of H_b, H_j, and H_g as a function of concentration at pH 9.0, 7.0, and 5.0 with the fitting curves are shown in Figures 3 and S19a. The obtained values of K and CAC are summarized in Table 1.

*EPR Spectra of **TEMPO-UBD** in Buffer Solution.* X-band (ν_0 = 9.4 GHz) ESR measurements at various concentrations (0.1−2.0 mM) were performed at pH 9.0, 7.0, and 5.0. In the lowest concentration of 0.1 mM **TEMPO-UBD** solution at pH 9.0, peaks with three well-resolved lines due to splitting of the nucleus spin of an N atom were observed at g = 2.0048 (Figure 4). The peak in the highest field showed the weaker intensity and slight broadening compared to those typical TEMPO analogues, indicating that the slow rotational correlation time (τ_R) took place even at 0.1 mM due to the large molecular size of **TEMPO-UBD**. As the concentration increased, the peak in the highest field became slightly weaker and broadened above 0.76 mM.

To evaluate the global motions of molecules and local motion of TEMPO moiety below and above 0.76 mM, τ_R values using Kivelson's equation[24] were estimated as 2.05 × 10^{-10} and 2.34 × 10^{-10} s, respectively (Figures 4 and S20 and eq S3). The resulting values above 0.76 mM were 16 and 1.1 times larger than those of typical TEMPO (1.5 × 10^{-11} s) and the solution of **TEMPO-UBD** below 0.76 mM, suggesting the formation of aggregate as seen for **H-UBD** and the inflection concentration implied the CAC value of **TEMPO-UBD** at pH 9.0. At pH 7.0 and 5.0, furthermore, the inflection points of τ_R values were both observed at the similar concentration of 0.66 mM. Even though similar CAC values between pH 9.0, 7.0, and 5.0 were observed, the estimated τ_R values showed a large difference. Below and above CAC at pH 7.0 and 5.0, the τ_R values were 1.85 and 2.09 × 10^{-10} s for pH 7.0 and 1.77 and 2.04 × 10^{-10} s for pH 5.0, respectively. Below and above CAC, the obtained τ_R values increased in the order pH 9.0 > 7.0 > 5.0. Below CAC, **TEMPO-UBD** in pH 5.0 solution exists as cationic monomer protonated at the tertiary N atoms, to give the fast molecular motion and smallest τ_R values due to Coulomb repulsion, while in pH 9.0 solution, the monomer of **TEMPO-UBD** exists as a neutral form and showed the largest τ_R values compared to those at pH 7.0 and 5.0. Above CAC, the resulting aggregate including Coulomb repulsion in an acidic condition also gave faster molecular motion and smaller τ_R values. In addition, the neutral aggregate gave slower molecular motion and larger τ_R values. Comparing the CAC values estimated from ^{1}H NMR for **H-UBD** and ESR for **TEMPO-UBD**, the values of **TEMPO-UBD** were smaller than those of **H-UBD**, indicating that the association constant (K) of **TEMPO-UBD** might be higher than that for **H-UBD**. The difference of the self-assembly behaviors among UBDs is responsible for the hydrophobicity of TEMPO moiety. ESR spectra of **TEMPO-UBD** in 2.0−0.1 mM buffer solutions at pH

DOI: 10.1021/acs.joc.6b01509
J. Org. Chem. 2016, 81, 8351−8362

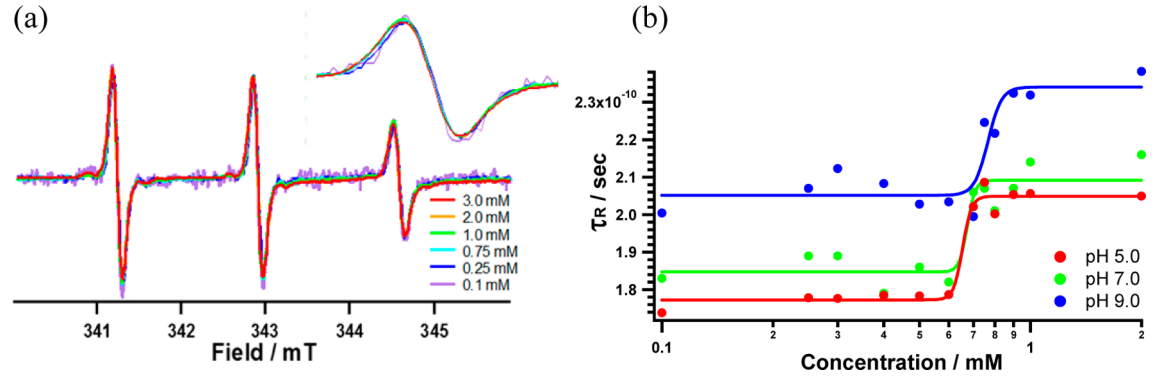

Figure 4. (a) Normalized ESR spectra of **TEMPO-UBD** in 2.0−0.1 mM buffer solutions at pH 9.0. Spectra were normalized by intensity at center peaks. Inset shows a magnified peaks at highest field. (b) Plots of τ_R values estimated by Kivelson's equation vs concentration at given pHs. The colored solid line indicates the sigmoidal fitting as a guide.

9.0, 7.0, and 5.0 are shown in Figures 4a and S21 (S15). Plots of τ_R vs concentration at pH 9.0, 7.0, and 5.0 are shown in Figure 4b. The τ_R values obtained under various conditions are summarized in Table 2.

Table 2. Values of τ_R (s) Estimated from Kivelson's Equation and CAC under Various Concentration Conditions at pH 9.0, 7.0, and 5.0

	τ_R (10^{-10} s)		
pH	below CAC	above CAC	CAC (mM)
9.0	2.05	2.34	0.76
7.0	1.85	2.09	0.66
5.0	1.77	2.04	0.66

Thermal Behaviors of H- and TEMPO-UBD in Water and Buffer Solution. *Transmittance Change of H- and TEMPO-UBDs by Heating Process.* We previously reported that the UBDs carrying the OEGs showed thermal responsiveness in an aqueous solution, to give a cloudy solution with LCST by heating.[11] This behavior is based on the dehydration surrounding OEGs in response to temperature, such that the self-assembly is accelerated by the increase of hydrophobicity of the molecules as well as the increasing size of the aggregate. To understand the thermal behavior of **H-** and **TEMPO-UBD**, the transmittance at 800 nm was monitored in the range 20−70 °C at various pHs.

In the case of 5 mM **H-UBD** solution at pH 9.0, which is above CAC, the transparent solution turned abruptly cloudy at 48 °C, which corresponds to the LCST value, and the resulting cloudy solution was maintained over 70 °C (Figure 5a). In contrast, the solution at 0.1 mM, which is below CAC, showed no LCST behavior until 70 °C, indicating a dependency on concentration. Similarly, the thermal behaviors in 5 mM buffer solution at various pH conditions were tested: LCST behavior at 63 °C and no LCST behavior until 70 °C, the same as for the dilute solution, were observed at pH 7.0 and 5.0, respectively. As the pH values decreased, the LCST became higher in the order pH 9.0 < 7.0 < 5.0, indicating that aggregates including the cation moiety in acidic conditions cannot easily form a large size aggregate and/or the amount of the aggregate is maintained. This is because Coulomb repulsion between cationic species took place by itself and/or the cationic species showed a large hydrophilicity than under basic conditions.

In the case of **TEMPO-UBD** in phosphate buffer solutions, interestingly, two-step decreases of the transmittance were

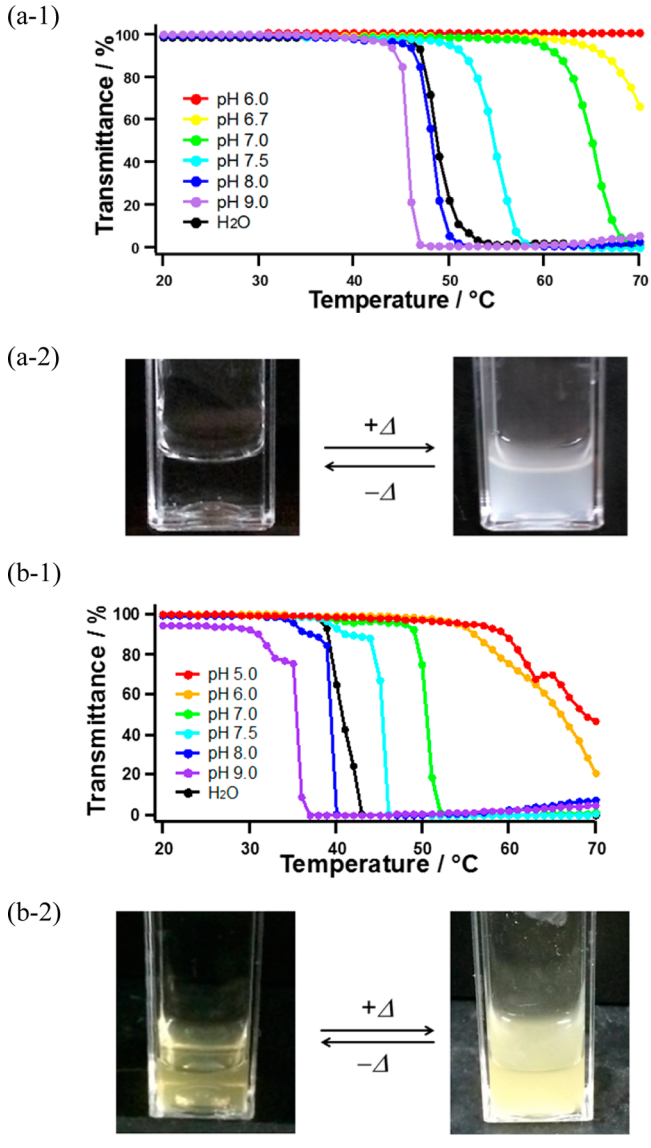

Figure 5. Thermal responsiveness monitored by changes of the transmittance at 800 nm in 5 mM aqueous solutions of (a) **H-UBD** and (b) **TEMPO-UBD** at given pHs and in pure water condition (black). The pictures indicate the change between transparent and turbid solutions in vials by thermal stimulus (5 mM at pH 7.0).

DOI: 10.1021/acs.joc.6b01509
J. Org. Chem. 2016, 81, 8351−8362

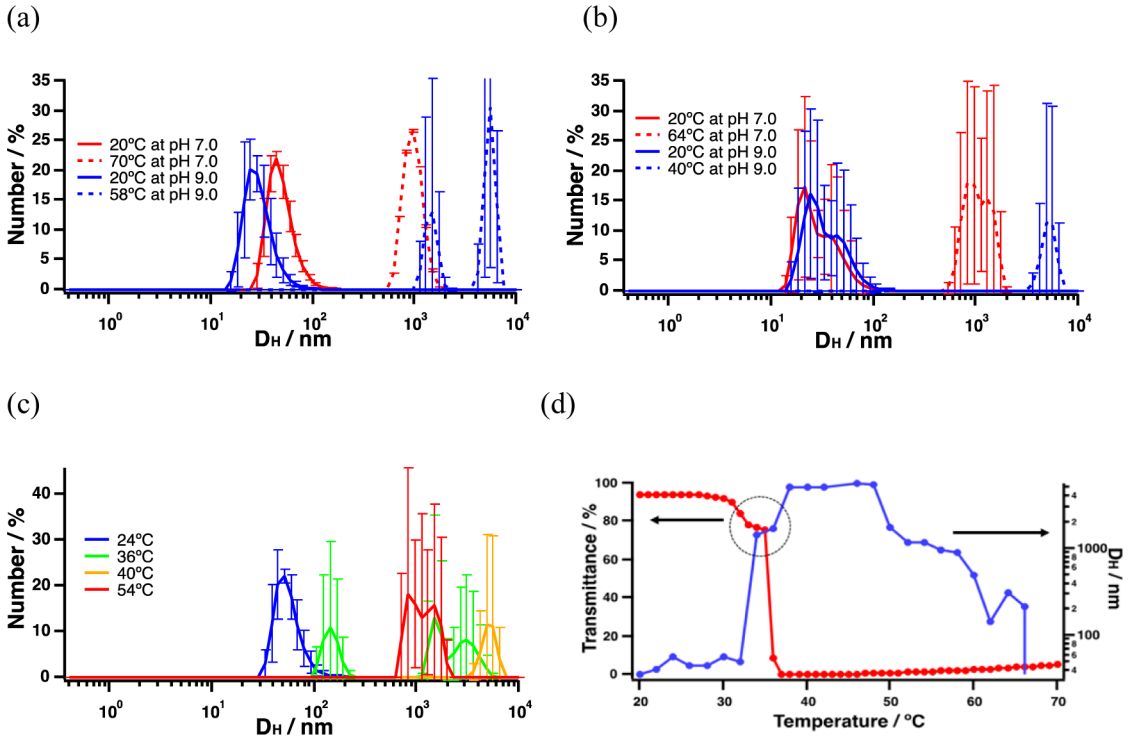

Figure 6. VT-DLS measurement in 5 mM buffer solutions. D_H values of (a) **H-UBD** and (b) **TEMPO-UBD** for given conditions of temperatures and pHs. (c) Detailed changes of D_H values at various temperature at pH 9.0 for **TEMPO-UBD**. (d) Plots of the average D_H value (right axis and blue mark) and transmittance (left axis and red mark) change vs temperature at pH 9.0 for **TEMPO-UBD**. Dotted circle in (d) represents the steady step between the first and second LCST behaviors.

observed (Figure 5b). At pH 9.0, the first and second steps began at 31 and 37 °C, respectively. The former step showed gradual change of the transmittance from 98 to 83%, and the latter step changed abruptly from 83 to 0%. Similar two-step LCST behaviors were observed at pH 8.0 and 7.0. This two-step behavior has been reported in the case of polymer compounds and was classified as "double LCST behavior".[25] It was noted that this thermal double-LCST behavior is the first such example among the supra-molecule category. Furthermore, it was found that the missing double-LCST behavior took place in the conditions using a pure water solution, and in the case of **H-UBD** even at a high concentration.

The abrupt decrease of the transmittance observed in the second step corresponds to the typical LCST behavior due to self-assembly by the dehydration surrounding OEGs. The gradual decrease of the transmittance observed in the first step might be led by the demetalation and consequently the self-assembly process in buffer solution including the salts of NaCl and KCl. Above 50 °C, in addition, a gradual increase of the transmittance occurred until 70 °C, suggesting the formation of precipitation due to a stronger dehydration effect. Actually, small precipitations in a cuvette were observed during the measurement at 70 °C. Comparing the LCST behavior between **H-** and **TEMPO- UBD**, the LCST value of **TEMPO-UBD** shifted to a lower temperature in the same conditions, suggesting that the hydrophobicity in the aggregates consisting of **TEMPO- UBD** was higher than in those of **H-UBD**. The reason for no double-LCST behavior in the **H-UBD** might be the differences in hydrophobicity and stability for the aggregate in buffer solution. The thermal responsiveness monitored by changes of the transmittance at 800 nm in 5 mM aqueous solutions of **H-** and **TEMPO-UBD** at given pHs, in addition in pure water, is shown in Figures 5 and S22 (S16). The thermal variations between transparent and turbid solutions into vials were photographed and are represented in Figure 5.

*Variable-Temperature DLS Measurements of **H-** and **TEMPO-UBD** in a Buffer Solution.* To understand the size of aggregate as well as the thermal self-assembly accompanying LCST, variable-temperature dynamic light scattering (VT-DLS) measurements in 5 mM of aqueous solutions were performed for **H-** and **TEMPO-UBD,** respectively. Each hydrodynamic diameter (D_H) was estimated as the average of three time measurements. The 5 mM solutions were selected as the concentration forms the aggregate in both **UBDs** derivatives.

In a buffer solution at pH 9.0 for **H-UBD** (Figure 6a), single broadening peaks corresponding to D_H values of 10−80 and over 1000 nm were observed at 20 and 58 °C, respectively, indicating that the aggregate below LCST was nanoparticles 10−80 nm in size and the grown aggregate above LCST was microparticles over 1000 nm in size. In the neutral condition (Figure 6a), similar D_H values of 20−100 and ∼1000 nm at pH 7.0 were observed below (20 °C) and above LCST (70 °C), indicating that nanoparticles and microparticles were formed below and above LCST. In addition, the pH dependence was negligible (Table 4). Even in pure water, the resulting D_H values were consistent with those in buffer solution (Figure S22). In contrast, in **TEMPO-UBD** with pH 9.0 solution (Figure 6b,c), which had the double-LCST behavior at 31 and 37 °C (Figure 5 and Table 3), the D_H values at 24 and 36 °C showed 30−150 nm as a single broadening peak and two broadening peaks at ∼300 and over 1000 nm, respectively, suggesting that nanoparticles 30−150 nm in size, as for **H-UBD**, and grown particles over 100 nm in size were formed below and above the first LCST step. Above the second LCST of

DOI: 10.1021/acs.joc.6b01509
J. Org. Chem. 2016, 81, 8351−8362

Table 3. LCST Values of H- and TEMPO-UBD under Various pH Conditions

	LCST value (°C)	
pH	H-UBD	TEMPO-UBD
9.0	45	31[a]
		37[b]
8.0	47	36[a]
		40[b]
7.0	63	42[a]
		51[b]
6.0	N.D.	56
5.0	–	64
water	48	39

[a]First LCST step. [b]Second LCST step.

40 °C, all particles exhibited over 1000 nm in size, and the resulting thermal behavior was consistent with those of **H-UBD**.

To reveal the relationship between the transmittance and D_H value, the D_H values changed by the heating process were plotted as a function of the temperature accompanied by the transmittance change (Figure 6d). As the temperature increased from 20 to 48 °C, two noncontinuous D_H values increases were observed at 32 and 36 °C, suggesting that changes in particle size took place at the same temperature as the double-LCST behavior obtained from the thermal transmittance change (left axis in Figure 6d). As the temperature increased above 48 °C, a decrease of the microparticle size was observed. This behavior occurred due to the formation of precipitations by a stronger dehydration effect (*vide supra*). At pH 7.0 and in pure water for **TEMPO-UBD** (Figures 6b and S23), comparable size changes with pH 9.0 were observed below and above LCST. Comparing the size of the particles between **H-** and **TEMPO-UBD**, even though **TEMPO-UBD** introduced a TEMPO moiety into **H-UBD**, no considerable difference in the particle size below and above LCST was seen. The obtained D_H values of **H-** and **TEMPO-UBD** under variable temperature and pH are shown in Figure 6a,b and are summarized in Table 4. The detailed changes of D_H values at various temperatures at pH 9.0 for **TEMPO-UBD** are shown in Figure 6c. Plots of D_H value (right axis) and transmittance (left axis) change vs temperature at pH 9.0 for **TEMPO-UBD** are given in Figure 6d.

*TEM and SEM images of **H-** and **TEMPO UBD**.* To identify the morphologies of the solution samples, transmission electron microscopy (TEM) was carried out, and stained images for **H-** and **TEMPO-UBD** were obtained. In addition, scanning electron microscopy (SEM) for **TEMPO-UBD** was performed. In TEM, the 5 mM water solution samples were mounted as 5 μL on a carbon grid with hydrophilic treatment, and the residual solution was sucked up by a filter paper at 23 °C for the sample below LCST. In contrast, the residual solution was evaporated at 70 °C for the sample above LCST. Each sample was stained with 5% uranyl acetate solution for the negative stained images. The salts often prevented observation of the morphology for organic materials even after staining, so the samples prepared in pure waters solution were used. In SEM, the samples were prepared by freeze-drying below LCST, while heating to 100 °C on hot plate for the samples above LCST. Each sample was coated with Pt moisture on a carbon tape onto a stage.

TEM. In **H-UBD**, spherical nanoparticles 20−60 nm in size were obtained below LCST, while amorphous-like assembly of over 100 nm in size were observed in the samples above LCST (Figures 7a and S25). The sizes obtained below and above LCST were slightly smaller than those obtained from DLS measurements. This suggests that the samples in solution included water molecules, making the sizes of samples obtained by DLS larger compared to those on TEM images. In the case of **TEMPO-**

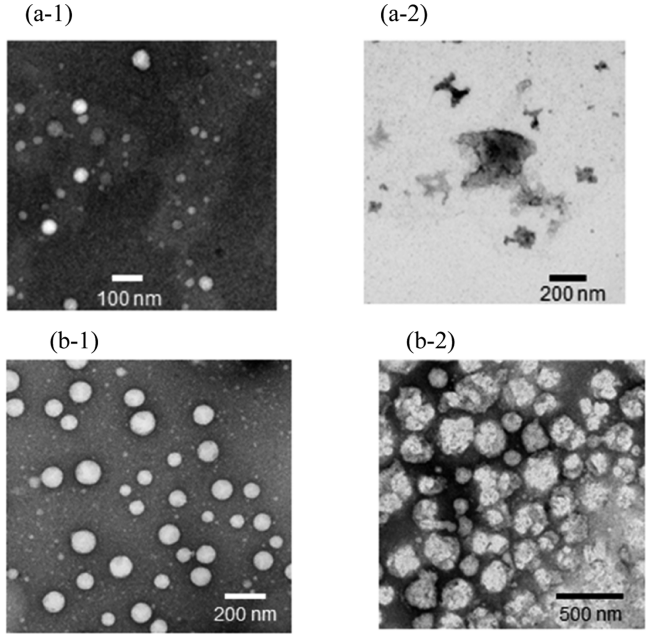

Figure 7. TEM images of (a) **H-** and (b) **TEMPO-UBD** prepared at (1) 23 and (2) 70 °C. Scale bars indicate (a-1) 100, (a-2) 200, (b-1) 200, and (b-2) 500 nm, respectively.

Table 4. Temperature and pH Dependencies of the Size Obtained from DLS for H- and TEMPO-UBD with 5 mM Buffer Conditions[a]

	size/nm (°C)					
	H-UBD			TEMPO-UBD		
temperature ranges (°C)	pH 9.0	pH 7.0	pure water	pH 9.0	pH 7.0	pure water
20	10−80	20−100	7−60	10−150	10−150	20−150
21−30				30−150 (24)		
31−40				100 (36), 3000 (40)		
41−50				∼1000 (50)		
51−69	∼1000 (58)			100 (60)	∼1000 (68)	
70		∼1000	∼700			∼1000

[a]The parentheses indicate the temperature recorded DLS data.

DOI: 10.1021/acs.joc.6b01509
J. Org. Chem. 2016, 81, 8351−8362

UBD (Figures 7b and S25), the sample below LCST showed spherical nanoparticles with 10−150 nm sizes same as **H-UBD**. In contrast, the samples above LCST exhibited formation of assemblies consisting of nanoparticles of sizes 300−500 nm. The resulting sizes below and above LCST were smaller than those estimated from DLS measurement for the same reason as with **H-UBD**. Above LCST, interestingly, a distinguishable morphology difference between **H-** and **TEMPO-UBD**, being amorphous-like particles and assemblies of the nanoparticles, was clearly observed.

SEM. In the sample after freeze-drying **TEMPO-UBD**, many spherical nanoparticles ∼60 nm in size were clearly observed. In contrast, the image of sample heated at 100 °C showed the grown particles with 100−500 nm in size and looked like the disordered amorphous shape, even though the TEM image gave the ordered assemblies consisting of nanoparticles. This discrepancy might result from melting the particles on a hot plate while preparing the SEM sample. TEM images and plots of count vs diameter for **H-** and **TEMPO-UBD** are shown in Figure 7a,b and S25. SEM images for **TEMPO-UBD** are shown in Figure S26.

*Structured Differences of Self-Assembly between **H-** and **TEMPO-UBD**.* While comparing the thermal properties and the morphologies of **H-** and **TEMPO-UBD**, interestingly, we observed distinguishable differences in the LCST behavior, and the morphology above LCST was observed. With respect to the LCST behaviors, double-LCST behavior was observed only in the case of **TEMPO-UBD**. Furthermore, the morphology of the microparticles obtained above LCST was different with the microparticle being disordered amorphous or ordered assemblies of nanoparticles in **H-** and **TEMPO-UBD**, respectively. These results suggest that different thermal self-assembly behaviors took place by different mechanisms at the molecular level. Below LCST, the nanoparticles of both **H-** and **TEMPO-UBD** were hydrated with many water molecules and metal ions at OEGs in the buffer solution. As the temperature increased, initially demetalation and then dehydration surrounding OEGs took place, creating more hydrophobicity at the molecule level and in grown microparticles. In the case of the **H-UBD** sample (Figure 8a), upon heating, the spherical ∼100 nm sized nanoparticles collapse, and the resulting amorphous microparticles might form a disordered random monomer. Although **UBDs** are supramolecules, the microparticles formed a globule-like structure, as also reported in thermoresponsive water-soluble polymers such as PNIPAM.[26] In the case of the **TEMPO-UBD** (Figure 8b), in contrast, the spherical nanoparticles 20−150 nm in size, obtained below LCST, accumulated by themselves and maintained their morphology and size even at 70 °C, to give new particles of micrometer order. Since the hydrophobicity of **TEMPO-UBD** is higher than that of **H-UBD**, the stability of the nanoparticles composing **TEMPO-UBD** in aqueous solution is also higher than that of **H-UBD**, so a difference in morphology change took place in both **UBDs** over LCST. With respect to the double-LCST behavior in **TEMPO-UBD**, we consider that the first and the second steps of LCST correspond to the demetalation and dehydration processes, respectively (Figure 8b). Even though the conditions were similar, the absence of double-LCST behavior in **H-UBD** is likely led by the weaker association constant of the nanoparticles, and so disordered microparticles (globules) were observed. The plausible structures and thermal mechanism of **H-** and **TEMPO-UBD** in buffer solution are shown in Figure 8.

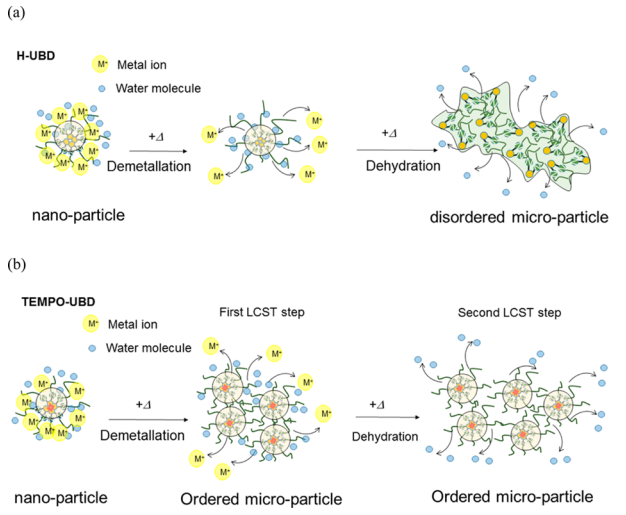

Figure 8. Schematic drawing of plausible structures of (a) **H-** and (b) **TEMPO-UBD** in buffer solution.

Water-Proton Longitudinal and Transverse Relaxivity (r_1 and r_2) and MR Imaging of TEMPO-UBD in Aqueous Conditions at pH 9.0, 7.0, and 5.0. To reveal the potential of **TEMPO-UBD** as a MRI contrast agent, water-proton relaxivites, r_1 and r_2, were determined from relaxation times, T_1 and T_2, obtained using 7 T MRI apparatus at various concentrations and at pH 9.0, 7.0, and 5.0, respectively. In addition, T_1- and T_2-weighted images were acquired (Figure 10). Considering bioimaging applications, the T_1 and T_2 values were obtained at 23 °C maintained using a gradient coil cooling system and air conditioners. Samples at 10.0, 7.5, 5.0, 3.3, 2.5, 1.0, 0.5, 0.25, and 0.125 mM were prepared in PCR tubes and used. The values of r_1 and r_2 were estimated from the slopes in the plots of T_1^{-1} or T_2^{-1} vs concentration. To evaluate the r_1 and r_2 values of **TEMPO-UBD**, the values were compared with simple TEMPO derivatives of **Oxo-TEMPO**.

The plots of relaxation rate, T_1^{-1} or T_2^{-1} at pH 7.0 vs concentration are shown in Figure 9. There were two different slopes, below and above 1.0 mM. Using the τ_R value estimated from ESR at pH 9.0, nanoparticles formed above the CAC value of 0.76 mM, which is consistent with the inflection values of 1 mM of r_1 and r_2. The values below and above CAC of r_1 were 0.14 and 0.18 mM^{-1} s^{-1}, respectively. In addition, **Oxo-TEMPO** showed no inflection point from 10−0.1 mM and an r_1 value of 0.15 mM^{-1} s^{-1}, suggesting that above CAC **TEMPO-UBD** exhibited a 1.2 times larger value than below CAC and **Oxo-TEMPO**, respectively. This result indicates that nanoparticles exhibited larger r_1 values due to the suppression of fast molecular motion, as expected. Similarly, at pH 7.0 and 5.0, inflection concentration of r_1 value was observed and was consistent with the value obtained from τ_R. The resulting r_1 values below and above CAC were 0.17 and 0.21 mM^{-1} s^{-1} at pH 7.0 and 0.15 and 0.19 mM^{-1} s^{-1} at pH 5.0, respectively. In the r_2 values estimated from T_2-weighted images, r_2 values above CAC were 0.28, 0.33, and 0.39 mM^{-1} s^{-1}, at pH 5.0, 7.0, and 9.0, respectively, suggesting a strong pH dependency. The reference of **Oxo-TEMPO** showed a smaller value of 0.19 mM^{-1} s^{-1}. As pH increased, the r_2 value increased in the order of pH 9.0 > 7.0 > 5.0, and the resulting r_2 values were larger than that of the reference. Since the r_2 value is directly affected by the spin quantum number and the amount of spin number compared to r_1, the aggregate number of nanoparticles at pH 9.0 might be the largest, and in the order pH 9.0 > 7.0 > 5.0. Plots of T_1^{-1} and T_2^{-1} vs concentration for **TEMPO-UBD** with **Oxo-TEMPO** at pH 9.0, 7.0, and 5.0 are

DOI: 10.1021/acs.joc.6b01509
J. Org. Chem. 2016, 81, 8351−8362

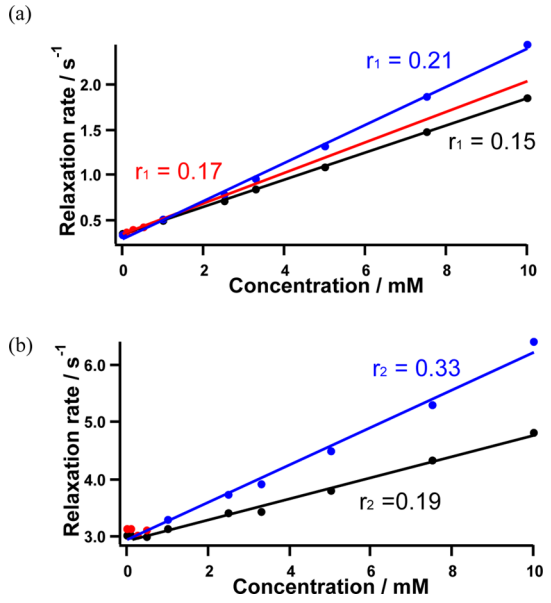

Figure 9. Plots of (a) T_1^{-1} and (b) T_2^{-1} vs concentration for **TEMPO-UBD** (blue and red) and **oxo-TEMPO** (black) at pH 7.0. The ranges for higher (10.0−1.0 mM) and lower (0.5−0 mM) concentrations of **TEMPO-UBD** are shown blue and red solid circles, respectively. The solid lines indicate the least-squares fitting of each slope.

shown in Figures 9 and Figure S27a,b. T_1- and T_2-weighted images at pH 7.0 are shown in Figure 10. The values of r_1 and r_2 at pH 9.0, 7.0, and 5.0 are summarized in Table 5.

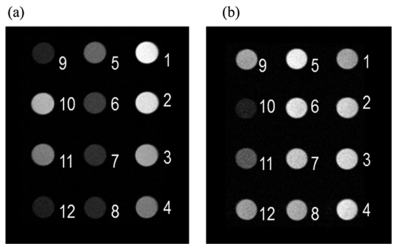

Figure 10. (a) T_1- and (b) T_2-weighted images of **TEMPO-UBD** at pH 7.0 and at various concentrations with standard materials. The numbers next to each image indicate the samples for (1) 10.0, (2) 7.5, (3) 5.0, (4) 3.3, (5) 2.5, (6) 1.0, (7) 0.5, (8) 0.25, and (9) 0.125 mM of **TEMPO-UBD**; (10) 0.25 and (11) 0.125 mM of $MnCl_2$; and (12) pure water, respectively.

Comparing the r_1 values above CAC at various pHs, the highest value was obtained in the neutral condition at pH 7.0 in spite of the highest τ_R value being seen at pH 9.0. This discrepancy between r_1 and τ_R values can be explained as follows. In the acidic condition at pH 5.0, the nanoparticles showed smaller τ_R values in ESR because the nanoparticles were carrying a cationic moiety, to lead a fast local motion of TEMPO moiety and/or fast global motion of the nanoparticles due to Coulomb repulsion. While in the basic condition at pH 9.0, even though the nanoparticles showed a larger τ_R value in ESR, the number of water molecules surrounding the TEMPO moiety is smaller owing to deprotonated tertiary N atoms and stronger hydrophobicity in the molecule. In the neutral condition at pH 7.0, even though the nanoparticle showed a smaller τ_R value than those at pH 9.0, many water molecules exist surrounding TEMPO moiety so the largest r_1 values were observed due to optimized conditions. Plausible molecular motions and environments of water molecules in nanoparticles comprising **TEMPO-UBD** at pH 9.0, 7.0, and 5.0 are shown in Figure 11.

Table 5. Values of r_1 and r_2 for TEMPO-UBD in Buffer Solutions under Various Conditions and a Blood Solution at pH 7.0 with Results of Oxo-TEMPO as Reference

		TEMPO-UBD	
pH		r_1 (mM^{-1} s^{-1})	r_2 (mM^{-1} s^{-1})
9.0	above CAC	0.18	0.39
	below CAC	0.14	0.21
7.0	above CAC	0.21	0.33
		0.24[a]	0.56[a]
		0.24[b]	0.38[b]
	below CAC	0.17	N.D.
		0.20[a]	0.88[a]
		0.17[b]	0.25[b]
5.0	above CAC	0.19	0.28
	below CAC	0.15	0.22
		Oxo-TEMPO	
		0.15	0.19

[a]Measured under blood solution. [b]After annealed at 70 °C and measured 25 °C.

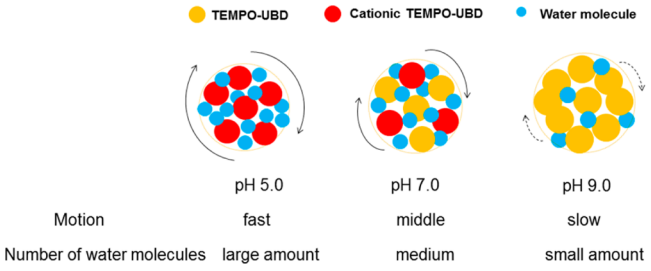

Figure 11. Schematic drawing of plausible molecular motions and environments of water molecules in nanoparticles comprising **TEMO-UBD** at pH 9.0, 7.0, and 5.0.

For bioimaging, furthermore, the stability of **TEMPO-UBD** in blood was confirmed by the variation of values of relaxivities (r_1 and r_2). The resulting values of r_1 and r_2 were 1.2 and 1.8 times larger than those in buffer solution at pH 7.0, suggesting that **TEMPO-UBD** was not labile in the blood and showed resistance against reductants such as ascorbic acid[27] and glutathione[28] in blood. The reason for the increase of relaxivities might be the interaction between proteins such as albumin and increased size.[29] Surprisingly, increased values of r_1 and r_2 were also observed even with annealing treatment of the sample to 70 °C. This result suggested that the heating process creates on the optimized formation of nanoparticles for the increase of relaxivities and/or the water molecules reoriented into **TEMPO-UBD**. Plots of T_1^{-1} and T_2^{-1} vs concentration for **TEMPO-UBD** in blood are shown in Figure S28, and values are summarized in Table 5.

CONCLUSION

In conclusion, we prepared a supra-molecular organic radical, **TEMPO-UBD**, carrying a TEMPO radical as a candidate metal-free MRI contrast agent. **TEMPO-UBD** showed thermal and pH responsiveness in addition to MR function. In buffer solutions above CAC, **TEMPO-UBD** formed a spherical nanoparticle 20−150 nm in size. These nanoparticles exhibited a two step "double LCST" thermoresponsive behavior and turned into micro-

DOI: 10.1021/acs.joc.6b01509
J. Org. Chem. 2016, 81, 8351−8362

particles above LCST. This double LCST is the first example among supra-molecules. As pH decreased, LCST values increased due to the formation of cationic **TEMPO-UBD**. To evaluate its potential as an MRI contrast agent, water-proton relaxivites, r_1 and r_2, were estimated under various pH conditions. The resulting r_1 and r_2 at pH 7.0 were 1.2 and 3 times larger than those of **Oxo-TEMPO**, indicating that an effective molecular size effect took place. In a blood sample, the relaxivities of r_1 and r_2 were 1.2 and 1.8 times larger than those in buffer solutions, indicating that **TEMPO-UBD** is not labile in a blood and thus is useful for bioimaging. *In vivo* imaging using **TEMPO-UBD** is under investigation. In the present stage, no extremely large r_1 and r_2 values, such as the nanoparticles, consisted of oligonucleotide-TEMPO system[9] were observed. Two insufficient factors to increase the r_1 and r_2 values were raised in the **TEMPO-UBD**. One is insufficient suppression of tumbling the TEMPO moiety, another one is fewer numbers of water molecules surrounding the TEMPO. To prepare candidate MRI contrast agents having larger r_1 and r_2 values using nanoparticles, thus, the design and preparation of radicals introducing the polar moiety, such as OEGs, hydroxyl, and carboxylic acid neighboring the radical center, are in progress.

EXPERIMENTAL SECTION

General Information. Infrared and UV−vis spectra were recorded. ^{1}H and ^{13}CNMR spectra were measured using $CDCl_3$ or DMSO-d_6 or D_2O including TMS or DDS as standard material. HRMS using ESI mass spectra (ESI MS) were recorded. ESR spectra were recorded on X-band (9.4 GHz) spectrometer equipped with a microwave frequency counter. Sample solutions in phosphate buffer were placed in capillary tubes and were measured at 25 °C. DLS measurements were performed. The images of TEM images were obtained. The sample mounted on a carbon grid with hydrophilic treatment was stained with 5% uranyl acetate aq. SEM was carried out. The samples were coated by Pt moisture by an ion coater and immobilized on a carbon tape onto a stage.

Relaxivity Measurements. The longitudinal (spin−lattice) and transverse (spin−spin) relaxation times (T_1 and T_2, respectively) were obtained on 25 MHz (0.59 T). The sample solutions (ca. 0.1−0.7 mM) in phosphate buffer were placed in 10 mm o.d. glass tubes and were measured at 25 °C. The values of relaxivity, r_1 and r_2, were calculated with eqs 1 and 2:

$$1/T_1 = 1/T_0 + r_1C \quad (1)$$

$$1/T_2 = 1/T_0 + r_2C \quad (2)$$

where T_0 and C are the relaxation time in the absence of the paramagnetic species and the concentration of the paramagnetic species, respectively.

***T*$_1$- and *T*$_2$-Weighted MRI for Samples.** MRI acquisitions of contrast agents were performed on a 7.0 T-MRI scanner with a volume coil (35 mm inner-diameter, transmission, and reception). Aqueous solution of contrast agents (150 μL) was put into a polymerization chain reaction (PCR) tube cluster plate. The PCR tube cluster plate was set in the center of the volume coil. Sample temperature was maintained at 23.0 ± 0.5 °C throughout all experiments using a gradient coil cooling system and air conditioners. MRI scanner, horizontal single-slice T_1-weighted MR images were acquired with the following parameters: spin echo, TR/TE = 400/9.6 ms, slice thickness = 2.0 mm, matrix = 256 × 256, field of view (FOV) = 38.4 × 38.4 mm^2, number of averages (NA) = 1, number of slices = 1. For longitudinal relaxation time (T_1) and longitudinal relaxivity (r_1) calculations, horizontal single-slice inversion−recovery MRI was obtained using RARE (rapid acquisition with relaxation enhancement) acquisition with the following parameters: TR = 10,000 ms, TE = 20 ms, inversion time = 52, 100, 200, 400, 800, 1600, 3200, 6400 ms, matrix size = 128 × 128, FOV = 38.4 × 38.4 mm^2, slice thickness = 2.0 mm, RARE factor = 4, and NA = 1.

Materials. Unless otherwise stated, the solvent and reagents were used without the purification. 2-Aminoethanol, 1,6-dibromohexane, 5-amino-1,3-isophthalicacid, potassium phthalimide, isophthaloyl chloride, and **Oxo-TEMPO** were purchased and used without purification. 2-(2-(2-methoxyethoxy)ethoxy)ethyl 4-methylbenzenesulfonate (**Eg$_3$Ts**) and tetramethyl-4-(4,4,5,5-tetramethyl-1,3,2-dioxaborolan-2-yl)-3,6-dihydropyridin-1(2*H*)-yloxyl radical were prepared according to the literatures.[14,16] TLC was performed on silica gel plates 60 F_{254} (Merck).

*11-(2-(2-(2-Methoxyethoxy)ethoxy)ethyl)-2,5,8-trioxa-11-azatridecan-13-ol (**TEG$_2$EA**).* To a solution of **Eg$_3$Ts** 33 g (0.10 mol) and 2-aminoethanol (2.5 g, 40 mmol) in 50 mL $CHCN_3$ was added K_2CO_3 (25g, 0.18 mol) and refluxed for 6 h. The solution was cooled to rt, and the residual was removed by suction. The resulting solution was evaporated under reduced pressure. The crude residual was chromatographed on silica gel using with $CHCl_3$:MeOH (100:1−50:1) as eluent to afford a colorless oil (10.8 g, 30.6 mmol) in 75% yield. IR (NaCl, cm^{-1}) 3472, 2873, 1456, 1352, 1294, 1245, 1200, 1108, 1045; ^{1}H NMR ($CDCl_3$, 500 MHz) δ 3.67−3.60 (*m*, 12H), 3.59−3.51 (*m*, 10H), 3.38 (*s*, 6H), 2.79 (*t*, *J* = 5.7 Hz, 4H), 2.72 (*t*, *J* = 5.0 Hz, 2H); ^{13}C NMR ($CDCl_3$) δ 71.9, 70.6, 70.5, 70.4, 69.8, 59.5, 59.0, 56.8, 54.2; ESI-MS *m*/*z* 354.25 [M + H] $^+$; HRMS (ESI) Calcd for $C_{16}H_{36}NO_7$ [M + H]$^+$: 354.2486, Found: 354.2519.

*2-((6-Bromohexyl)oxy)-N,N-bis(2-(2-(2-methoxyethoxy)ethoxy)-ethyl)ethan-1-amine (**Eg$_3$NEg$_3$C$_6$Br**).* To a solution of 1,6-dibromohexane (14.5 g, 59.4 mmol) in dist. THF (25 mL) was added a solution of NaH (1.5 g, 64 mmol) in dist. THF in an ice bath and stirred for several minutes. To the solution was added dropwise **TEG$_2$EA** (7.3 g, 21 mmol) in dist. THF (10 mL) and stirred overnight. To the reaction mixture was added sat. NH_4Cl aqueous, and the mixture was extracted with Et_2O three times. The combined organic layer was dried over $MgSO_4$, evaporated under reduced pressure, and the crude residual was chromatographed on silica gel using a mixture of $CHCl_3$:MeOH (100:1−50:1) as the eluent to afford a colorless oil (7.22 g, 14.0 mmol) in 68% yield. IR (NaCl, cm^{-1}) 2932, 2864, 1457, 1352, 1300, 1245, 1199, 1114, 1029; ^{1}H NMR ($CDCl_3$, 500 MHz) δ 3.66−3.63 (*m*, 8H), 3.62−3.59 (*m*, 4H), 3.56−3.52 (*m*, 8H), 3.48 (*t*, *J* = 6.2 Hz, 2H), 3.42−3.39 (*m*, 4H), 3.38 (*s*, 6H), 2.80−2.75 (*m*, 6H), 1.86 (*quin*, *J* = 7.1 Hz, 2H), 1.57 (*quin*, *J* = 7.0 Hz, 2H), 1.45 (*quin*, *J* = 6.9 Hz, 2H), 1.36 (*quin*, *J* = 6.9 Hz, 2H); ^{13}C NMR ($CDCl_3$) δ 72.0, 71.0, 70.6, 70.6, 70.4, 69.8, 69.4, 59.1, 54.7, 54.6, 33.9, 32.7, 29.5, 28.0, 25.4; ESI-MS *m*/*z* 538.23 [M + Na]$^+$; HRMS (ESI) Calcd for $C_{22}H_{46}BrNNaO_7$ [M + Na]$^+$: 538.2350, Found: 538.2317.

*2-(11-(2-(2-(2-Methoxyet)hoxy)ethoxy)ethyl)-2,5,8,14-tetraoxa-11-azaicosan-20-yl)isoindoline-1,3-dione (**Eg$_3$NEg$_3$C$_6$Pht**).* A solution of **Eg$_3$NEg$_3$C$_6$Br** (7.22 g, 14.0 mmol) and potassium phthalimide (3.9 g, 21 mmol) in DMF (60 mL) was stirred at 110 °C for 4 h. To the reaction mixture was added water and extracted with Et_2O three times. The combined organic layer was dried over $MgSO_4$ and evaporated under reduced pressure. The crude residual was chromatographed on silica gel using $CHCl_3$:MeOH (100:1−50:1) as the elute to afford a colorless oil (6.48 g, 11.1 mmol) in 80% yield. IR (NaCl, cm^{-1}) 2932, 2863, 1772, 1714, 1467, 1436, 1396, 1369, 1301, 1249, 1199, 1113; ^{1}H NMR ($CDCl_3$, 500 MHz) δ 7.84 (*d*, *J* = 5.4 Hz, 2H), 7.71(*d*, *J* = 5.4 Hz, 2H), 3.68 (*t*, *J* = 7.3 Hz, 2H), 3.65−3.59 (*m*, 12H), 3.56−3.53 (*m*, 8H), 3.40−3.38 (*m*, 8H), 2.80−2.74 (*m*, 6H), 1.68 (*quin*, *J* = 6.8 Hz, 2H), 1.55 (*quin*, *J* = 6.6 Hz, 2H), 1.47−1.35 (*m*, 4H); ^{13}C NMR ($CDCl_3$, 126 MHz) δ 168.4, 133.9, 132.2, 123.2, 72.0, 71.1, 70.6, 70.6, 70.4, 69.8, 69.4, 59.0, 54.7, 54.6, 38.0, 29.6, 28.6, 26.7, 25.8; ESI-MS *m*/*z* 605.34 [M + Na]$^+$; HRMS (ESI) Calcd for $C_{30}H_{50}N_2NaO_9$ [M + Na]$^+$: 605.3409, Found: 605.3377.

*6-((11-(2-(2-(2-Methoxyethoxy)ethoxy)ethyl)-2,5,8-trioxa-11-azatridecan-13-yl)oxy)hexan-1-amine (**Eg$_3$NEg$_3$C$_6$NH$_2$**).* To a solution of **Eg$_3$NEg$_3$C$_6$Pht** (6.5 g, 11 mmol) in EtOH (130 mL) was added dropwise hydrazine monohydrate (2.2 g, 44 mmol) and refluxed for 4 h. The reaction mixture was evaporated under reduced pressure, and the crude residual was diffused with Et_2O. The insoluble mixture in Et_2O was removed by suction filtration, and the filtrate was evaporated. The crude residual was chromatographed on silica gel using $CHCl_3$:MeOH (100:1−50:1 with 5% trimethylamine) to afford a colorless oil (3.92 g, 8.65 mmol) in 78% yield. IR (NaCl, cm^{-1}) 3371, 2929, 2862, 1577,

DOI: 10.1021/acs.joc.6b01509
J. Org. Chem. 2016, 81, 8351−8362

1458, 1351, 1328, 1303, 1249, 1199, 1113; ^{1}H NMR ($CDCl_3$, 500 MHz) δ 3.65−3.62 (*m*, 8H), 3.61−3.59 (*m*, 4H), 3.56−3.52 (*m*, 8H), 3.48 (*t*, *J* = 6.2 Hz, 2H), 3.40 (*t*, *J* = 6.7 Hz, 2H), 3.38 (*s*, 6H), 2.80−2.75 (*m*, 6H), 2.68 (*t*, *J* = 7.0 Hz, 2H), 1.56 (*quin*, *J* = 6.6 Hz, 2H), 1.44 (*quin*, *J* = 6.7 Hz, 2H), 1.38−1.30 (*m*, 4H); ^{13}C NMR ($CDCl_3$, 126 MHz) δ 72.0, 71.2, 70.7, 70.6, 70.4, 69.8, 69.4, 59.1, 54.7, 54.6, 42.2, 33.7, 29.7, 26.7, 26.1; ESI-MS *m*/*z* 453.35 $[M + H]^+$; HRMS (ESI) Calcd for $C_{22}H_{49}N_2O_7$ $[M + H]^+$: 453.3534, Found: 453.3505.

*1,1′-(5-Iodo-1,3-phenylene)bis(3-(11-(2-(2-(2-methoxyethoxy)-ethoxy)ethyl)-2,5,8,14-tetraoxa-11-azaicosan-20-yl)urea) (**Iodo-UBD**).* A solution of 5-iodoisophthalic acid (584 mg, 2 mmol) in $SOCl_2$ (30 mL) was refluxed for 2 h and evaporated under reduced pressure, to afford a crude 5-iodoisophthaloyl chloride. To a solution of the crude mixture in THF (4 mL) was added NaN_3 (860 mg, 13 mmol) in a water solution and stirred in an ice bath for 2 h. To the mixed solution was added sat. $NaHCO_3$ solution and extracted with toluene three times. The combined organic layer was dried over $MgSO_4$ and evaporated under reduced pressure until 15 mL, to afford a toluene solution of 5-iodoisophthaloyl diazide. Without purification, the crude reaction mixture was refluxed for 2 h, to afford a toluene solution including 1-iodo-3,5-diisocyanatobenzene. To a solution of 1-iodo-3,5-diisocyanatobenzene in toluene was added dropwise **$Eg_3NEg_3C_6NH_2$** (2.0 g, 4.4 mmol) in 8 mL CH_2Cl_2 in an ice bath and stirred overnight at rt. The reaction mixture was evaporated under reduced pressure, and the crude residual was chromatographed on silica gel using $CHCl_3$: MeOH (100:1−50:1) as eluent to afford a yellowish oil (1.45 g, 1.22 mmol) in 61%. The reactions of 5-iodoisophthaloyl dichloride, 5-iodoisophthaloyl diazide, and 1-iodo-3,5-diisocyanatobenzene were monitored by IR spectra, respectively. IR (NaCl, cm^{-1}) 3491, 3340, 2930, 2864, 1695, 1594, 1538, 1449, 1351, 1305, 1261, 1201, 1111 1028; ^{1}H NMR (DMSO-d_6, 500 MHz) δ 8.44 (*s*, 2H), 7.45 (*d*, *J* = 1.8 Hz, 2H), 7.28 (*t*, *J* = 1.8 Hz, 1H), 6.06 (*t*, *J* = 5.6 Hz, 2H), 3.51−3.46 (*m*, 24H), 3.44−3.41 (*m*, 16H), 3.40−3.35 (*m*, 8H), 3.23 (*s*, 12H), 3.04 (*q*, *J* = 6.4 Hz, 4H), 2.65 (*t*, *J* = 6.2 Hz, 12H), 1.48 (*quin*, *J* = 6.7 Hz, 4H), 1.41 (*quin*, *J* = 6.7 Hz, 4H), 1.32−1.26 (*m*, 8H), ^{13}C NMR (DMSO-d_6, 126 MHz) δ 155.3, 142.6, 119.0, 106.1, 95.0, 79.6, 71.8, 70.6, 70.3, 70.2, 70.1, 69.7, 66.8, 58.5, 54.6, 30.1, 29.7, 26.7, 25.9, ESI-MS *m*/*z* 596.32 $[M+2H]^{2+}$, HRMS (ESI) Calcd for $C_{52}H_{101}N_6O_{16}I$ $[M + 2H]^{2+}$: 596.3154, Found: 596.3154.

*1,1′-(1,3-Phenylene)bis(3-(11-(2-(2-(2-methoxyethoxy)ethoxy)-ethyl)-2,5,8,14-tetraoxa-11-azaicosan-20-yl)urea) (**H-UBD**).* **H-UBD** was prepared in a manner similar to **Iodo-UBD** using isophthaloyl chloride in place of 5-iodoisophthaloyl chloride. A yellowish oil (1.6 g, 1.5 mmol) was obtained in 76% yield. IR (NaCl, cm^{-1}) 3502, 3346, 2931, 2863, 1689, 1606, 1549, 1482, 1455, 1421, 1351, 1302, 1238, 1201, 1110, 1028; ^{1}H NMR (DMSO-d_6, 500 MHz) δ 8.31 (*s*, 2H), 7.43 (*t*, *J* = 1.8 Hz, 1H), 7.01 (*t*, *J* = 8.0 Hz, 1H), 6.93 (*dd*, *J* = 1.8 Hz, 8.0 Hz, 2H), 6.00 (*t*, *J* = 5.6 Hz, 2H), 3.48−3.51 (*m*, 24H), 3.38−3.44 (*m*, 20H), 3.32−3.36 (*m*, 4H), 3.23 (*s*, 12H), 3.05 (*q*, *J* = 6.5 Hz, 4H), 2.65 (*t*, *J* = 6.1 Hz, 12H), 1.48 (*quin*, *J* = 6.7 Hz, 4H), 1.40 (*quin*, *J* = 6.7 Hz, 4H), 1.33−1.29 (*m*, 8H); ^{13}C NMR ($CDCl_3$, 126 MHz) δ 155.6, 141.4, 129.2, 110.8, 107.2, 79.7, 71.8, 70.6, 70.3, 70.2, 70.1, 69.7, 69.5, 58.5, 54.6, 30.2, 29.7, 26.7, 26.0; ESI-MS *m*/*z* 533.37 $[M+2H]^{2+}$; HRMS (ESI) Calcd for $C_{52}H_{102}N_6O_{16}$ $[M + 2H]^{2+}$: 533.3671, Found: 533.3696.

*1,1′-(5-(1-Oyl-2,2,6,6-tetramethyl-3-dihydropyridin-4-yl)benzene-1,3-diyl)bis(3-(11-(2-(2-(2-methoxyethoxy)ethoxy)ethyl)-2,5,8,14-tetraoxa-11-azaicosan-20-yl)urea) (**TEMPO-UBD**).* **Iodo-UBD** (596 mg, 0.5 mmol), $Pd(PPh_3)_4$ (28.9 mg, 0.025 mmol), 2,2,6,6-tetramethyl-4-(4,4,5,5-tetramethyl-1,3,2-dioxaborolan-2-yl)-3,6-dihydropyridin-1(2*H*)-yloxyl radical (168 mg, 0.6 mmol), and degassed 1,4-dioxane (4 mL) were placed in a three neck flask, and a bubbling treatment of the mixed solution using N_2 gas was carried out carefully for 30 min. To the reaction mixture was added 10% Na_2CO_3 aq. and stirred at 100 °C for 6 h. Brine was added to the reaction mixture and was extracted with $CHCl_3$ three times, and the combined organic layer was dried over $MgSO_4$ and then evaporated under reduced pressure. The crude residual was chromatographed on silica gel using $CHCl_3$:MeOH (100:1−50:1) as elute to afford a brown wax-like solid (344 mg, 0.28 mmol) in 57% yield; IR (NaCl, cm^{-1}) 3516, 3339, 2929, 2862, 1696, 1668, 1602, 1558, 1453, 1360, 1249, 1201, 1114, 1033, 850; ^{1}H NMR (DMSO-d_6 + ascorbic acid, 500 MHz) δ 8.34 (*s*, 2H), 7.29 (*t*, *J* = 1.7 Hz, 1H), 7.04 (*d*, *J* = 1.7 Hz, 2H), 5.98 (*t*, *J* = 5.6 Hz, 2H), 5.78 (*s*, 1H), 3.52−3.47 (m, 44H), 3.36 (*t*, J = 6.4 Hz, 4H), 3.23 (*s*, 12H), 3.05 (*q*, *J* = 6.4 Hz, 4H), 2.30 (*s*, 2H), 1.49 (*quin*, *J* = 6.7 Hz, 4H), 1.41 (*quin*, *J* = 6.7 Hz, 4H), 1.33−1.27 (*m*, 8H), 1.20 (*s*, 6H), 1.12 (*s*, 6H); ^{13}C NMR (DMSO-d_6 + ascorbic acid, 126 MHz) δ 155.6, 141.6, 141.3, 131.8, 130.2, 107.8, 105.9, 91.8, 88.4, 73.7, 71.7, 70.7, 70.2, 70.0, 68.4, 58.5, 54.3, 30.2, 29.6, 26.7, 25.9, ESI-MS *m*/*z* 609.42 $[M+2H]^{2+}$; HRMS (ESI) Calcd for $C_{61}H_{116}N_7O_{17}$ $[M + 2H]^{2+}$: 609.4208, Found: 609.4212.

■ ASSOCIATED CONTENT

Supporting Information

The Supporting Information is available free of charge on the ACS Publications website at DOI: 10.1021/acs.joc.6b01509.

Copies of ^{1}H- and ^{13}C NMR for new materials. Additional data of ^{1}H NMR spectra for **H-UBD** and ESR spectra for **TEMPO-UBD** in various aqueous conditions. Additional plots of the transmittance at 800 nm vs temperature, number vs D_H, and relaxation rate vs concentration for **H-** and **TEMPO-UBD** in various conditions (PDF)

■ AUTHOR INFORMATION

Corresponding Author

*E-mail: karasawa@phar.kyushu-u.ac.jp. Tel: +81-92-642-6593. Fax: +81-92-642-6545

Notes

The authors declare no competing financial interest.

■ ACKNOWLEDGMENTS

The authors thank Ms. Sayaka Shibata, Mr. Nobuhiro Nitta, and Yoshikazu Ozawa (National Institute of Radiological Sciences; NIRS, QST) for MRI operation. S.K. thanks Dr. Noboru Koga for many helpful discussions. This work was partially supported by Platform for Drug Discovery, Informatics, and Structural Life Science from the Ministry of Education, Culture, Sports, Science and Technology (MEXT), Japan, Grants-in-Aid for exploratory Research (no. 26620070) from the Japan Society for the Promotion of Science (JSPS), PRESTO program on Molecular Technology from Japan Science Technology Agency (JST). MR imaging and analysis are also financially supported by the Center of Innovation Program (COI) streams from JST and Jisedai/innovative cancer grants from Japan Agency for Medical Research and Development (AMED).

■ REFERENCES

(1) (a) Laurent, S.; Forge, D.; Port, M.; Roch, A.; Robic, C.; Elst, L. V.; Muller, R. N. *Chem. Rev.* **2008**, *108*, 2064−2110. (b) Hao, R.; Xing, R.; Xu, Z.; Hou, Y.; Gao, S.; Sun, S. *Adv. Mater.* **2010**, *22*, 2729−2742. (c) Gale, E. M.; Atanasova, I. P.; Blasi, F.; Ay, I.; Caravan, P. *J. Am. Chem. Soc.* **2015**, *137*, 15548−15557.

(2) (a) Della Rocca, J. D.; Liu, D.; Lin, W. *Acc. Chem. Res.* **2011**, *44*, 957−968. (b) Caravan, P.; Ellison, J. J.; McMurry, T. J.; Lauffer, R. B. *Chem. Rev.* **1999**, *99*, 2293−2352.

(3) (a) Baranyai, Z.; Pálinkás, Z.; Uggeri, F.; Maiocchi, A.; Aime, S.; Brücher, E. *Chem. - Eur. J.* **2012**, *18*, 16426−16435. (b) Frenzel, T.; Lengsfeld, P.; Schirmer, H.; Hütter, J.; Weinmann, H. J. *Invest. Radiol.* **2008**, *43*, 817−828.

(4) Kanda, T.; Ishii, K.; Kawaguchi, H.; Kitajima, K.; Takenaka, D. *Radiology* **2014**, *270*, 834−841.

(5) (a) Yamada, K. I.; Yamamiya, I.; Utsumi, H. *Free Radic. Res.* **2006**, *40*, S151. (b) Kuppusamy, P.; Ilangovan, G. H. L.; Cardounel, A. J.; Zweier, J. L.; Yamada, K.; Krishna, M. C.; Mitchell, J. B. *Cancer Res.* **2002**, *62*, 307−312.

DOI: 10.1021/acs.joc.6b01509
J. Org. Chem. 2016, 81, 8351−8362

(6) (a) Yamato, M.; Kudo, W.; Shiba, T.; Yamada, K. I.; Watanabe, T.; Utsumi, H. *Free Radical Res.* **2010**, *44*, 249−257. (b) Zhang, R. L.; Goldstein, S.; Samuni, A. *Free Radical Biol. Med.* **1999**, *26*, 1245−1252.
(7) (a) Cheng, Z.; Thorek, D. L. J.; Tsourkas, A. *Adv. Funct. Mater.* **2009**, *19*, 3753−3759. (b) Winalski, C. S.; Shorkroff, C. S.; Mulkern, R. V.; Schneider, E.; Rosen, G. M. *Magn. Reson. Med.* **2002**, *48*, 965−972. (c) Li, Y.; Lei, X.; Lawler, R. G.; Murata, Y.; Komatsu, K.; Turro, N. J. *J. Phys. Chem. Lett.* **2010**, *1*, 2135−2138.
(8) (a) Rajca, A.; Wang, Y.; Boska, M.; Paletta, J. T.; Olankitwanit, A.; Swanson, M. A.; Mitchell, D. G.; Eaton, S. S.; Eaton, G. R.; Rajca, S. *J. Am. Chem. Soc.* **2012**, *134*, 15724−15727. (b) Hayashi, H.; Karasawa, S.; Tanala, A.; Odoi, K.; Chikama, K.; Kuribayashi, H.; Koga, N. *Magn. Reson. Chem.* **2009**, *47*, 201−204. (c) Hayashi, H.; Karasawa, S.; Koga, N. *J. Org. Chem.* **2008**, *73*, 8683−8693.
(9) Tanimoto, E.; Karasawa, S.; Ueki, S.; Nitta, N.; Aoki, I.; Koga, N. *RSC Adv.* **2013**, *3*, 3531−3534.
(10) (a) Sato, Y.; Hayashi, H.; Okazaki, M.; Aso, M.; Karasawa, S.; Ueki, S.; Suemune, H.; Koga, N. *Magn. Reson. Chem.* **2008**, *46*, 1055−1058. (b) Okazaki, M.; Sato, Y.; Karasawa, S.; Koga, N. *Nucle, Acid, Symp, Ser.* **2008**, *52*, 375−376.
(11) Hayashi, H.; Ohkubo, K.; Karasawa, S.; Koga, N. *Langmuir* **2011**, *27*, 12709−12719.
(12) Tachaboonyakiat, W.; Ajiro, H.; Akashi, M. *Polym. J.* **2013**, *45*, 971−978.
(13) (a) Betancourt, J. E.; Rivera, J. M. *Langmuir* **2015**, *31*, 2095−2103. (b) Arai, M.; Ito, K. *Chem. Lett.* **2015**, *44*, 1416−1418. (c) Harada, A.; Takashima, Y.; Nakahata, M. *Acc. Chem. Res.* **2014**, *47*, 2128−2140. (d) Liong, M.; Lu, J.; Kovochich, M.; Xia, T.; Ruehm, S. G.; Nel, A. E.; Tamanoi, F.; Zink, J. I. *ACS Nano* **2008**, *2*, 889−896.
(14) Manfredi, N.; Cecconi, B.; Calabrese, V.; Minotti, A.; Peri, F.; Ruffo, R.; Monai, M.; Romero-Ocaña; Montini, T.; Fornasiero, P.; Abbotto, A. *Chem. Commun.* **2016**, *52*, 6977−6980.
(15) (a) Iwanaga, T.; Ogawa, M.; Yamauchi, T.; Toyota, S. *J. Org. Chem.* **2016**, *81*, 4076−4080. (b) Raders, S. M.; Moore, J. N.; Parks, J. K.; Miller, A. D.; Leißing, T. M.; Kelley, S. P.; Rogers, R. D.; Shaughnessy, K. H. *J. Org. Chem.* **2013**, *78*, 4649−4664.
(16) Kálai, T.; Jekö, J.; Berente, Z.; Hideg, K. *Synthesis* **2006**, *3*, 439−446.
(17) Tataurova, Y.; Sealy, M. J.; Larsen, R. G.; Larsen, S. C. *J. Phys. Chem. Lett.* **2012**, *3*, 425−429.
(18) Kakehashi, R.; Shizuma, M.; Yamamura, S.; Maeda, H. *J. Colloid Interface Sci.* **2005**, *289*, 498−503.
(19) (a) Li, Z.; Chen, C.; Gröger, S.; Kressler, J. *Polymer* **2012**, *53*, 2613−2618. (b) Seco, J. M.; Latypov, S. K.; Quiñoá, E.; Riguera, R. *J. Org. Chem.* **1997**, *62*, 7569−7574.
(20) (a) Fielding, L. A.; Lane, J. A.; Derry, M. J.; Mykhaylyk, O. O.; Armes, S. P. *J. Am. Chem. Soc.* **2014**, *136*, 5790−5798. (b) Hosono, N.; Gillissen, M. A. J.; Li, Y.; Sheiko, S. S.; Palmans, A. R. A.; Meijer, E. W. *J. Am. Chem. Soc.* **2013**, *135*, 501−510.
(21) Mousseau, J. J.; Xing, L.; Tang, N.; Cuccia, L. A. *Chem. - Eur. J.* **2009**, *15*, 10030−10038.
(22) Ponnuswamy, N.; Pantoş, G. D.; Smulders, M. M. J.; Sanders, J. K. M. *J. Am. Chem. Soc.* **2012**, *134*, 566−573.
(23) de Greef, T. F. A.; Smulders, M. M. J.; Wolffs, M.; Schenning, A. P. J.; Sijbesma, R. P.; Meijer, E. W. *Chem. Rev.* **2009**, *109*, 5687−5754.
(24) (a) Kundu, K.; Das, R. *Mol. Phys.* **2014**, *112*, 1577−1588. (b) Kivelson, D. *J. Chem. Phys.* **1966**, *45*, 1324.
(25) (a) Liang, X.; Liu, F.; Kozlovskaya, V.; Palchak, Z.; Kharlampieva, E. *ACS Macro Lett.* **2015**, *4*, 308−311. (b) Chen, X. L.; Sun, H.; Xu, J.; Han, X.; Liu, H. L.; Hu, Y. *RSC Adv.* **2015**, *5*, 86584−86592.
(26) Heyda, J.; Soll, S.; Yuan, J.; Dzubiella, J. *Macromolecules* **2014**, *47*, 2096−2102.
(27) (a) Eggersdorfer, M.; Laudert, D.; Létinolis, U.; McClymont, T.; Medlock, J.; Netschere, T.; Bonrath, W. *Angew. Chem., Int. Ed.* **2012**, *51*, 12960−12990. (b) Packer, J. E.; Slater, T. F.; Willson, R. L. *Nature* **1979**, *278*, 737−738.
(28) (a) Banhegyi, G.; Braun, L.; Csala, M.; Puskas, F. *Free Radical Biol. Med.* **1997**, *23*, 793−803. (b) Braun, L.; Puskas, F.; Csala, M.; Meszaros, G.; Mandl, J.; Banhegyi, G. *Free Radical Biol. Med.* **1997**, *23*, 804−808. (c) Basu, S.; Som, S.; Deb, S.; Mukherjee, D.; Chatterjee, I. B. *Biochem. Biophys. Res. Commun.* **1979**, *90*, 1335−1340.
(29) Goswami, L. N.; Cai, Q.; Ma, L.; Jalisatgi, S. S.; Hawthorne, M. F. *Org. Biomol. Chem.* **2015**, *13*, 8912−8918.

DOI: 10.1021/acs.joc.6b01509
J. Org. Chem. 2016, 81, 8351−8362